

Probing Chemical Enrichment in Extremely Metal-Poor Galaxies

KEITA FUKUSHIMA ^{1,2} KENTARO NAGAMINE ^{1,3,4,5,6} AKINORI MATSUMOTO,^{7,8} YUKI ISOBE ^{7,8}
MASAMI OUCHI ^{9,7,10} TAKAYUKI R. SAITOH ¹¹ AND YUTAKA HIRAI ^{12,13}

- ¹Theoretical Astrophysics, Department of Earth and Space Science, Graduate School of Science, Osaka University, 1-1 Machikaneyama, Toyonaka, Osaka 560-0043, Japan
- ²Waseda Research Institute for Science and Engineering, Faculty of Science and Engineering, Waseda University, 3-4-1 Okubo, Shinjuku, Tokyo 169-8555, Japan
- ³Theoretical Joint Research Project, Forefront Research Center, Graduate School of Science, Osaka University, 1-1 Machikaneyama, Toyonaka, Osaka 560-0043, Japan
- ⁴Kavli IPMU (WPI), The University of Tokyo, 5-1-5 Kashiwanoha, Kashiwa, Chiba, 277-8583, Japan
- ⁵Department of Physics & Astronomy, University of Nevada, Las Vegas, 4505 S. Maryland Pkwy, Las Vegas, NV 89154-4002, USA
- ⁶Nevada Center for Astrophysics, University of Nevada, Las Vegas, 4505 S. Maryland Pkwy, Las Vegas, NV 89154-4002, USA
- ⁷Institute for Cosmic Ray Research, The University of Tokyo, 5-1-5 Kashiwanoha, Kashiwa, Chiba 277-8582, Japan
- ⁸Department of Physics, Graduate School of Science, The University of Tokyo, 7-3-1 Hongo, Bunkyo, Tokyo 113-0033, Japan
- ⁹National Astronomical Observatory of Japan, National Institutes of Natural Sciences, 2-21-1 Osawa, Mitaka, Tokyo 181-8588, Japan
- ¹⁰Kavli Institute for the Physics and Mathematics of the Universe (WPI), University of Tokyo, Kashiwa, Chiba 277-8583, Japan
- ¹¹Department of Planetology, Graduate School of Science, Kobe University, 1-1 Rokkodai-cho, Nada-ku, Kobe, Hyogo 657-8501, Japan
- ¹²Department of Physics and Astronomy, University of Notre Dame, 225 Nieuwland Science Hall, Notre Dame, IN 46556, USA
- ¹³Astronomical Institute, Tohoku University, 6-3 Aoba, Aramaki, Aoba-ku, Sendai, Miyagi 980-8578, Japan

ABSTRACT

The chemical composition of galaxies offers vital insights into their formation and evolution. A key aspect of this study is the correlation between helium abundance (He/H) and metallicity, which is instrumental in estimating the primordial helium produced during Big Bang nucleosynthesis. We investigate the chemical enrichment history of low-metallicity galaxies, with a particular focus on extremely metal-poor galaxies (EMPGs), using one-zone models. Our one-zone model, employing the [Limongi & Chieffi \(2018\)](#) yield, aligns well with observed high He/H ratios at low metallicities and successfully reproduces Fe/O ratios similar to those found in EMPGs. In contrast, the [Nomoto et al. \(2013\)](#) yield does not fully match the high Fe/O ratios observed in EMPGs. Furthermore, we explored models incorporating supermassive stars (SMS) as Pop III stars and intermittent star formation, both of which produced higher He/H ratios than the standard one-zone model. A model calculation that incorporates SMS yields effectively explain young galaxies ($< 10^8$ years) with metallicities $(\text{O}/\text{H}) \times 10^5 < 20$ and $\text{He}/\text{H} > 0.085$. Notably, the model, where the outer envelope of the SMS's CO core is completely ejected, achieves $\text{He}/\text{H} > 0.12$, aligning with the properties of high- z galaxies recently discovered by JWST. Additionally, these models predict high N/O, consistent with JWST observations in the early universe.

Keywords: galaxies: abundances — galaxies: dwarf — galaxies: high-redshift — galaxies: evolution — methods: numerical

1. INTRODUCTION

Galaxy evolution begins with the first galaxies, which also mark the initial sites of metal enrichment in the universe. Advanced cosmological hydrodynamic simulations indicate that these primordial galaxies, existing at redshifts greater than 10 ($z > 10$), are characterized by notably low metallicities ($Z = 0.01 - 0.001 Z_{\odot}$) and relatively low stellar masses ($M_{\star} \lesssim 10^6 M_{\odot}$) ([Wise et al.](#)

[2012](#); [Johnson et al. 2013](#); [Kimm & Cen 2014](#); [Romano-Díaz et al. 2014](#); [Yajima et al. 2017, 2023](#)).

The James Webb Space Telescope (JWST) has discovered galaxies at $z > 10$ with spectroscopic confirmation of redshifts ([Roberts-Borsani et al. 2023](#); [Williams et al. 2023](#); [Curtis-Lake et al. 2023](#); [Bunker et al. 2023](#); [Arrabal Haro et al. 2023a,b](#); [Harikane et al. 2024, 2023](#)), which also allow the investigation of mass-metallicity

relation (MZR) for high- z galaxies (Curti et al. 2023a; Nakajima et al. 2023). In particular, GN-z11, noted for its significant mass at high redshifts, has garnered considerable attention and been the focus of numerous detailed observational studies (Cameron et al. 2023; Bunker et al. 2023; Senchyna et al. 2023; Isobe et al. 2023).

However, observing low-mass galaxies in the early universe is still difficult without the aid of the gravitational lensing effect. Isobe et al. (2022) found that H α emission of galaxies with stellar masses of $M_\star \sim 10^6 M_\odot$ is only detected at $z < 1$ with JWST and up to $z < 2$ with forthcoming Thirty Meter Telescope (TMT) without the gravitational lensing effect (c.f. Vanzella et al. 2023).

The Extremely Metal-Poor Galaxies (EMPGs) could be the local analog of low-mass first galaxies, and might help to understand the properties of first galaxies. EMPGs have low stellar masses ($M_\star < 10^7 M_\odot$), low metallicities ($Z < 0.1 Z_\odot$), and high specific star formation rates (sSFR $\sim 100 \text{ Gyr}^{-1}$), which are similar to the characteristics of the first galaxies (Kojima et al. 2020). Curti et al. (2023b) examined the MZR for low-mass galaxies at $3 < z < 10$ observed using gravitational lensing effects and found it to be comparable to the MZR of nearby ‘Blueberry’ galaxies (Yang et al. 2017). Studying EMPGs provides a unique opportunity to decipher the formation history of the first galaxies.

The chemical evolution of EMPGs is poorly understood. High Fe/O close to the solar abundance has been observed for some EMPGs (Izotov et al. 2018a; Kojima et al. 2021). Chemical evolution model calculations (Isobe et al. 2022; Watanabe et al. 2023) suggest the need for brighter hypernovae and/or pair-instability supernovae (PISNe), which are caused by massive stars (Barkat et al. 1967; Heger & Woosley 2002; Umeda & Nomoto 2002; Nomoto et al. 2013). Furthermore, galaxies with high Fe abundance ($[\text{Fe}/\text{O}] = 0.3$) have been observed as early as $z = 10.60$, with attempts to explain this phenomenon using PISNe or bright hypernovae Nakane et al. (2024). This distinction is crucial, as young galaxies in the low-metallicity regime are often associated with a top-heavy initial mass function (IMF) (e.g. Kumari et al. 2018; Zou et al. 2024; Chon et al. 2021, 2022, 2023).

The abundance ratio He/H can be examined as a function of metallicity to estimate the primordial He abundance, but this relation is highly uncertain (Matsumoto et al. 2022). Vincenzo et al. (2019) show the relation between He/H and 12+O/H using a one-zone model and cosmological chemodynamical simulation. They compared Nomoto et al. (2013) and Limongi & Chieffi (2018) yield models for core-collapse supernovae (CCSNe), and

Karakas (2010) and Ventura et al. (2013) for asymptotic giant branch (AGB) yields. This showed that He/H was particularly high when using the Limongi & Chieffi (2018) yield, which considers the effect of the Wolf-Rayet star at the low-metallicity range.

Additionally, a supermassive star (SMS) could also be considered as the origin of high He/H in young galaxies. Yanagisawa et al. (2024) reported that the He/H ratios of three objects at $z = 5.92, 6.11,$ and 6.23 have $\text{He}/\text{H} > 0.1$ at $(\text{O}/\text{H}) \times 10^5 < 7$. This He/H value is higher than those observed in nearby dwarf galaxies (Hsyu et al. 2020) and EMPGs (Matsumoto et al. 2022). SMS is also gaining attention as a possible explanation for objects like GN-z11, which shows a high N/O ratio at high redshift (Charbonnel et al. 2023; Isobe et al. 2023; Nandal et al. 2024).

In this study, we aim to elucidate specific aspects of the formation and evolution of EMPGs and high- z galaxies. To do this, we use the one-zone model. The one-zone model was performed to understand the fundamental parameters that affect the evolution of galaxies with low metal abundances and young ages, such as EMPG galaxies and high- z galaxies, and the extent to which different yields alter chemical evolution.

This paper is organized as follows. Section 2 details our methodology, outlining the one-zone model. Section 3.1 focuses on assessing the effects of metallicity on He/H and Fe/O ratios in a one-zone model, considering two different yield models. Section 3.2 explores the impact of SMS and star formation history using one zone model. In Section 4.1 we discuss the chemical abundance of [N/O] and in Section 4.2 we discuss how primordial He abundance should be obtained using the observed galaxies. We then conclude in Section 5. Details of the one-zone model are described in Appendix A, and the basic results of the yield models by Nomoto et al. (2013); Limongi & Chieffi (2018); Nandal et al. (2024) are presented in Appendix B. In this study, we adopt the following solar abundance ratios: $\log(\text{Fe}/\text{O}) = -1.23$ and $\log(\text{N}/\text{O}) = -0.86$ (Asplund et al. 2021). The abundance ratios are expressed as values normalized to solar abundances, defined as follows: $[A/B] = \log_{10}((N_A/N_{A,\odot})/(N_B/N_{B,\odot}))$, where N_A and N_B represent the numbers of elements A and B, respectively. The subscripts $N_{A,\odot}$ and $N_{B,\odot}$ indicate the solar abundances for those elements. For He/H, we use the ratio $\text{He}/\text{H} = N_{\text{He}}/N_{\text{H}}$. Additionally, for O/H, we also use $(\text{O}/\text{H}) \times 10^5 = N_{\text{O}}/N_{\text{H}} \times 10^5$.

2. METHOD

We follow the calculation of the one-zone box model by Kobayashi & Taylor (2023) as our standard model;

see Appendix A for details. Here, we calculate the outflow rate depending on the energy injection from the stars, and the energy release rate calculated by CELIB code (Saitoh 2016, 2017). We run 400 model calculations, each focussing on different parameters to explore a range of scenarios. The varied parameters include the gas-depletion timescale t_{dep} , gas inflow timescale t_{in} , gas outflow rate f_o , and the fraction of metals in the inflowing gas f_{inf} . To provide a clear and organized overview of these models and their parameters, we summarize the details in Table 1.

Chemical evolution is computed using the CELIB code (Saitoh 2016, 2017), which incorporates the effects of CCSNe, type Ia supernovae (SN Ia), and AGB stars. The CCSNe yield of Nomoto et al. (2013), the SN Ia yields of Seitenzahl et al. (2013), the AGB star yields of Karakas (2010) and the super AGB star yields of Doherty et al. (2014) were used. The Chabrier (2003) IMF is adopted with a stellar mass range of 0.1–100 M_{\odot} . We also performed an additional calculation using the Limongi & Chieffi (2018) yields for CCSN specifically adopting the set R yields (all stars more massive than 25 M_{\odot} fully collapse to a black hole), as an alternative to the Nomoto et al. (2013) yields, facilitating a comparative analysis. In Limongi’s set R yields, three models with varying stellar rotation are provided, and the CELIB model selects the appropriate one based on an empirical relationship between stellar mass and rotation. Hereafter, we refer to the calculation using the Nomoto et al. (2013) yield for CCSN as Model-N, and the calculation using the Limongi & Chieffi (2018) yield as Model-L (Table 2).

We treat stars with $Z \leq 10^{-5} Z_{\odot}$ as Pop III, and adopt the following yield tables for Pop III stars: the CCSNe yield of Nomoto et al. (2013), the AGB star yields of Campbell & Lattanzio (2008) and Gil-Pons et al. (2013), and the top-heavy IMF from Susa et al. (2014). In the CCSNe yield of Pop III, we also include the contribution from PISN (Nomoto et al. 2013). A delay-time distribution function with a power law of t^{-1} was used for the SN Ia event rate (Totani et al. 2008; Maoz & Mannucci 2012; Maoz et al. 2014), which is turned on after 4×10^7 yr. The hypernovae mixing fraction f_{HN} is set to 0.05. The details of the above yield tables are given in Fukushima et al. (2023).

In our standard model, the star formation rate is given by the gas mass divided by the depletion time t_{dep} (see eq. A3); however, since we normalize the entire equation by the gas mass, the SFR has a units of 1/time. To assess the impact of Pop III stars potentially being SMS, we also implement an intermittent star formation model that forms an SMS with a mass of M_{SMS} only

Table 1. Summary of our one zone model parameters. See Appendix A for the definition of the parameters.

t_{dep} (yrs)	t_{in} (yrs)	f_o	f_{inf}
10^7	10^7	0.0	0.0
10^8	10^8	0.1	0.01
10^9	10^9	1.0	0.1
10^{10}	10^{10}	10	1.0
–	–	100	–

when the accumulated stellar mass at $Z_{\star} < 10^{-5} Z_{\odot}$ surpasses M_{SMS} . During this accumulation phase, we do not explicitly form stars, with sporadic star formation occurring only through the formation of SMS. Here, we adopt the yield model of $M_{\text{SMS}} = 6127 M_{\odot}$ from Nandal et al. (2024). We conduct calculations with two models: one where the outermost 10% of the total mass is ejected (Model-N&N-10%), and another where all mass outside the CO core is ejected (Model-N&N-CO).

Additionally, the models in which SMS directly collapse (DC) into black holes with the same yield are referred to as Model-N&N-10%-DC and Model-N&N-CO-DC, respectively.

For comparison, we also performed calculations using the same intermittent star formation model with the Nomoto et al. (2013) yield (Model-N_{int}). This mass of $M_{\text{SMS}} = 6127 M_{\odot}$ falls within the range of $1900 M_{\odot} < M_{\text{SMS}} < 8900 M_{\odot}$, identified by Nandal et al. (2024) as reproducing the N/O ratio observed in high- z galaxies.

As a summary of this section, Table 2 presents the yield sets, star formation, and DC considered in this study. When the metallicity of stars is the same, we use the same yield for both AGB stars and SNe Ia. However, in the Model-N&N series, which assumes SMS at $Z_{\star} < 10^{-5} Z_{\odot}$, all stars in the stellar cluster are considered to be SMS, so we do not use the yields for AGB stars and SNIa.

3. RESULT

3.1. Standard model

We start by presenting the chemical abundance from the standard one-zone model calculations. Figure 1 shows the (O/H) $\times 10^5$ –He/H relationship obtained from the one-zone model calculations of Model-N (*panel (a)*) and Model-L (*panel (b)*). The blue, green, red, and cyan lines represent $t_{\text{dep}} = 10$ Myr, 100 Myr, 1 Gyr, and 10 Gyr, respectively. The other parameters are set to $t_{\text{in}} = 1$ Gyr, $f_o = 0.1$, and $f_{\text{inf}} = 0.1$. The solid lines indicate the results using the CCSN, SNIa, and AGB yields, while the dashed lines indicate the results using only the CCSN yields.

Table 2. Summary of yield models used in this paper.

† For $Z_* < 10^{-5} Z_\odot$: AGB yield is from [Campbell & Lattanzio \(2008\)](#); [Gil-Pons et al. \(2013\)](#); SNIa yield is from [Seitenzahl et al. \(2013\)](#).

‡ For $Z_* \geq 10^{-5} Z_\odot$: AGB yield is from [Karakas \(2010\)](#); [Doherty et al. \(2014\)](#); SNIa yield is from [Seitenzahl et al. \(2013\)](#).

Model	$Z_* < 10^{-5} Z_\odot$ 0.7–300 M_\odot		$Z_* \geq 10^{-5} Z_\odot$ 0.1–100 M_\odot		SF	DC
	IMF: Susa et al. (2014)		IMF: Chabrier (2003)			
	CCSNe	AGB&SNIa†	CCSNe	AGB&SNIa‡		
N	Nomoto et al. (2013)	yes	Nomoto et al. (2013)	yes	continuous	no
N _{int}	Nomoto et al. (2013)	yes	Nomoto et al. (2013)	yes	intermittent	no
L	Limongi & Chieffi (2018)	yes	Limongi & Chieffi (2018)	yes	continuous	yes
N&N-10%	Nandal et al. (2024) (10%)	no	Nomoto et al. (2013)	yes	intermittent	no
N&N-10%-DC	Nandal et al. (2024) (10%)	no	Nomoto et al. (2013)	yes	intermittent	yes
N&N-CO	Nandal et al. (2024) (CO)	no	Nomoto et al. (2013)	yes	intermittent	no
N&N-CO-DC	Nandal et al. (2024) (CO)	no	Nomoto et al. (2013)	yes	intermittent	yes

In Model-N, the larger the t_{dep} , the steeper the slope of the solid line. For the dashed line without the AGB contribution, when $t_{\text{dep}} < 1$ Gyr, it shows an evolution similar to that of the solid line. However, for $t_{\text{dep}} \gtrsim 1$ Gyr, it indicates a lower He/H at the same $(\text{O}/\text{H}) \times 10^5$ compared to the solid line.

In Model-L, the solid line shows that the higher the t_{dep} , the higher He/H up to $(\text{O}/\text{H}) \times 10^5 < 12.5$, similar to Model-N. However, for $(\text{O}/\text{H}) \times 10^5 > 12.5$, the solid line for $t_{\text{dep}} = 1$ Gyr shows a higher He/H than the solid line for $t_{\text{dep}} = 10$ Gyr. Additionally, compared to Model-N, the solid lines for all t_{dep} show higher He/H for $(\text{O}/\text{H}) \times 10^5 < 20$. In the case of $t_{\text{dep}} = 10$ Myr, the dashed line and the solid line are consistent, as seen in *panel (a)*, but for $t_{\text{dep}} = 100$ Myr, the dashed line falls below the solid line at $(\text{O}/\text{H}) \times 10^5 \gtrsim 10$.

In both panels, the chemical enrichment progresses due to CCSNe when the solid and dashed lines are consistent. For the models that do not agree, oxygen is primarily provided by CCSNe, while He is mainly injected by AGB stars.

The results of the one-zone model calculations performed with the parameters listed in [Table 1](#) are shown in [Figure 2](#), plotted for each galaxy age. The left two panels (*a* and *c*) employ the [Nomoto et al. \(2013\)](#) yield to explore He/H and Fe/O ratios in relation to metallicity, respectively, while the right two panels (*b* and *d*) utilize the [Limongi & Chieffi \(2018\)](#) yield for a similar calculation. The circle, triangle, cross, and square symbols in the scatter plot indicate the different ages 10^6 , 10^7 , 10^8 , 10^9 , and 10^{10} yr of the one-zone galaxy since the beginning of star formation, respectively. The colors indicate the gas depletion timescale (t_{dep}), which is defined in the [Appendix A](#). The black line represents the evolutionary track for the case of

$(t_{\text{dep}}[\text{yr}], t_{\text{in}}[\text{yr}], f_o, f_{\text{inf}}) = (10^9, 10^{10}, 10, 0.01)$. The blue, red, green, and purple arrows indicate how the point on the track at 10^9 yr moves when the parameters are changed to $t_{\text{dep}} = 10^{10}$ yr, $t_{\text{in}} = 10^9$ yr, $f_o = 1$, and $f_{\text{inf}} = 0.1$, respectively. The red and purple arrows almost overlap; thus the red arrow has been made thicker and the purple arrow thinner for better visibility. The gas fraction ($= M_{\text{gas}} / (M_{\text{gas}} + M_{\text{star}})$) in 10^7 , 10^8 , 10^9 , and 10^{10} years for the black line are 0.995, 0.949, 0.575, and 0.076, respectively. In models characterized by short t_{dep} or high f_o , the calculation stops once their gas reservoirs are depleted. As a result, for certain samples, the data points at the $10^9 - 10^{10}$ year mark are not represented. In panels (*a*) and (*b*), the black dots are the observations of EMPGs ([Matsumoto et al. 2022](#)), and the gray dots are the observations of dwarf galaxies ([Hsyu et al. 2020](#)). The black dashed line is the linear fit, performed by [Matsumoto et al. \(2022\)](#). In panel (*c*) and (*d*), data points with black error bars show the chemical abundance of high- z galaxies ([Steidel et al. 2016](#); [Cullen et al. 2021](#); [Kashino et al. 2022](#); [Harikane et al. 2020](#); [Nakane et al. 2024](#)), while those with gray error bars represent low- z galaxies ([Izotov et al. 2018b](#); [Kojima et al. 2020, 2021](#); [Isobe et al. 2022](#)). The gray scattered data points represent MW stars ([Amarsi et al. 2019](#)).

In panel (*a*), our one-zone model shows a discrepancy with certain EMPG observations; notably, none of our model results exhibit He/H ratios lower than 0.082. This deviation mainly stems from the adoption of a higher primordial He abundance, as suggested by [Planck Collaboration et al. \(2016\)](#), compared to the He/H ratio at $(\text{O}/\text{H}) \times 10^5 = 0$ determined by [Matsumoto et al. \(2022\)](#). Additionally, the slope of our modeled He/H versus O/H relationship is shallower than that of the observed fitting line. This suggests that in our model, He enrichment

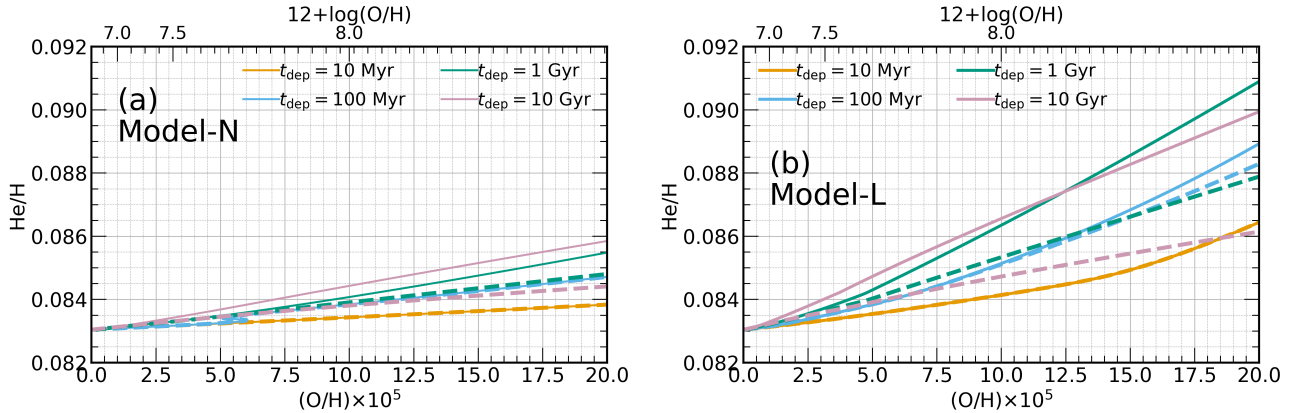


Figure 1. $(O/H) \times 10^5$ – He/H relationship obtained from the one-zone model calculations of Model-N (panel (a)) and Model-L (panel (b)). The blue, green, red, and cyan lines represent $t_{dep} = 10$ Myr, 100 Myr, 1 Gyr, and 10 Gyr, respectively. The solid lines indicate the results using CCSN, SNIa, and AGB yields, while the dashed lines indicate the results using only CCSN yields. In panel (a), the ages at which $(O/H) \times 10^5 = 20$ are 4.3×10^6 yr, 5.3×10^7 yr, 4.0×10^8 yr, and 2.8×10^9 yr for $t_{dep} = 10^7$, 10^8 , 10^9 , and 10^{10} yr, respectively. Additionally, in panel (b), the ages are 2.1×10^7 yr, 1.3×10^8 yr, 9.9×10^8 yr, and 6.1×10^9 yr for $t_{dep} = 10^7$, 10^8 , 10^9 , and 10^{10} yr, respectively.

from CCSNe and AGB stars has a limited impact on altering the He/H abundance ratio, largely due to the predominance of primordial gas in the galaxy’s composition as per our setup. Although He and oxygen are enriched by CCSNe, the He/H ratio in the CCSNe ejecta is at most around $He/H \sim 0.3$, which is only about 3.6 times higher than the primordial $He/H \sim 0.083$ (Appendix B). However, oxygen ejecta has a very high metallicity, with $12 + \log(O/H) \sim 11$, meaning that highly enriched gas is mixed into gas within the one-zone box. As a result, as seen in Fig. 1, the slope becomes very shallow, producing data points with $He/H \sim 0.083$ across a wide range of $(O/H) \times 10^5 = 0 - 15$, as seen in Fig. 2.

Looking at the black line, we can see that until 10^8 years, $He/H \sim 0.083$, but afterward the increase in metallicity stops and He/H becomes higher. At $t = 10^9$ years, where the black line’s t_{dep} is the same age, the gas fraction decreases to 0.575, and the effect of chemical enrichment becomes prominent. As seen in Fig. 7 of Appendix B, at 10^9 years, the phase where pollution from AGB stars dominates begins. The oxygen pollution from AGB stars is lower than that from CCSNe, and since He/H is higher, it creates a rise in $He/H > 0.083$ at $(O/H) \times 10^5 = 10$. Looking at the arrows, we can see that even when t_{in} is shortened from 10^{10} years to 10^9 years, if $t_{dep} \leq t_{in}$, the changes are only around $\Delta(O/H) \times 10^5 \sim 1$ and $\Delta He/H \sim 0.001$. Additionally, even when f_{inf} is increased by a factor of 10, the changes are of a similar magnitude to those when t_{in} is changed. However, when f_o is reduced by a factor of 10, no metal outflow occurs, and $\Delta(O/H) \times 10^5 > 10$, resulting in a significant increase in O/H .

In panel (b), similar to panel (a), we see that the He/H ratio does not fall below 0.082. For values of $(O/H) \times 10^5 \gtrsim 10$, our model achieves He/H ratios that are comparable to, or marginally lower than, the fitting line of the observation established by Matsumoto et al. (2022). As seen in Appendix B, the $12 + \log(O/H)$ released by CCSNe is $12 + \log(O/H) = 9 - 11$ for the Nomoto et al. (2013) yield (Model-N), whereas for the Limongi & Chieffi (2018) yield (Model-L), it only reaches a maximum of $12 + \log(O/H) = 10.5$. Additionally, for Model-L at $10^{6.8}$ years, stellar winds release gas with low metallicity, where $12 + \log(O/H) < 9$. In Model-L, the He/H released at this age is only about 0.3 times lower than that of Model-N, but since $12 + \log(O/H)$ is more than 100 times lower, the gas can retain high He/H at low O/H . The trend of the black line and arrows is the same as in panel (a). Although this yield model does not fully replicate the high He/H observations at low metal abundances noted by Hsyu et al. (2020), it shows the existence of parameters that align with the dashed line obtained by Matsumoto et al. (2022) for $(O/H) \times 10^5 \gtrsim 10$, as shown in panel (a). The 10^8 -yr-old galaxies with $(O/H) \times 10^5 = 5 - 10$ and $He/H = 0.087$ evolve along a track like the black line.

Several points in our model calculations match the fitting line from the observations (Matsumoto et al. 2022) at $(O/H) \times 10^5 > 10$ with a $\Delta He/H = 0.003$. Those with the same t_{dep} are clustered within a range of $\Delta((O/H) \times 10^5) = 5$ and $\Delta(He/H) = 0.001$, and their ages are the same as well. By looking at the arrows, it becomes clear that this group shares the same t_{in} and t_{dep} parameters, but has different f_o and f_{inf} param-

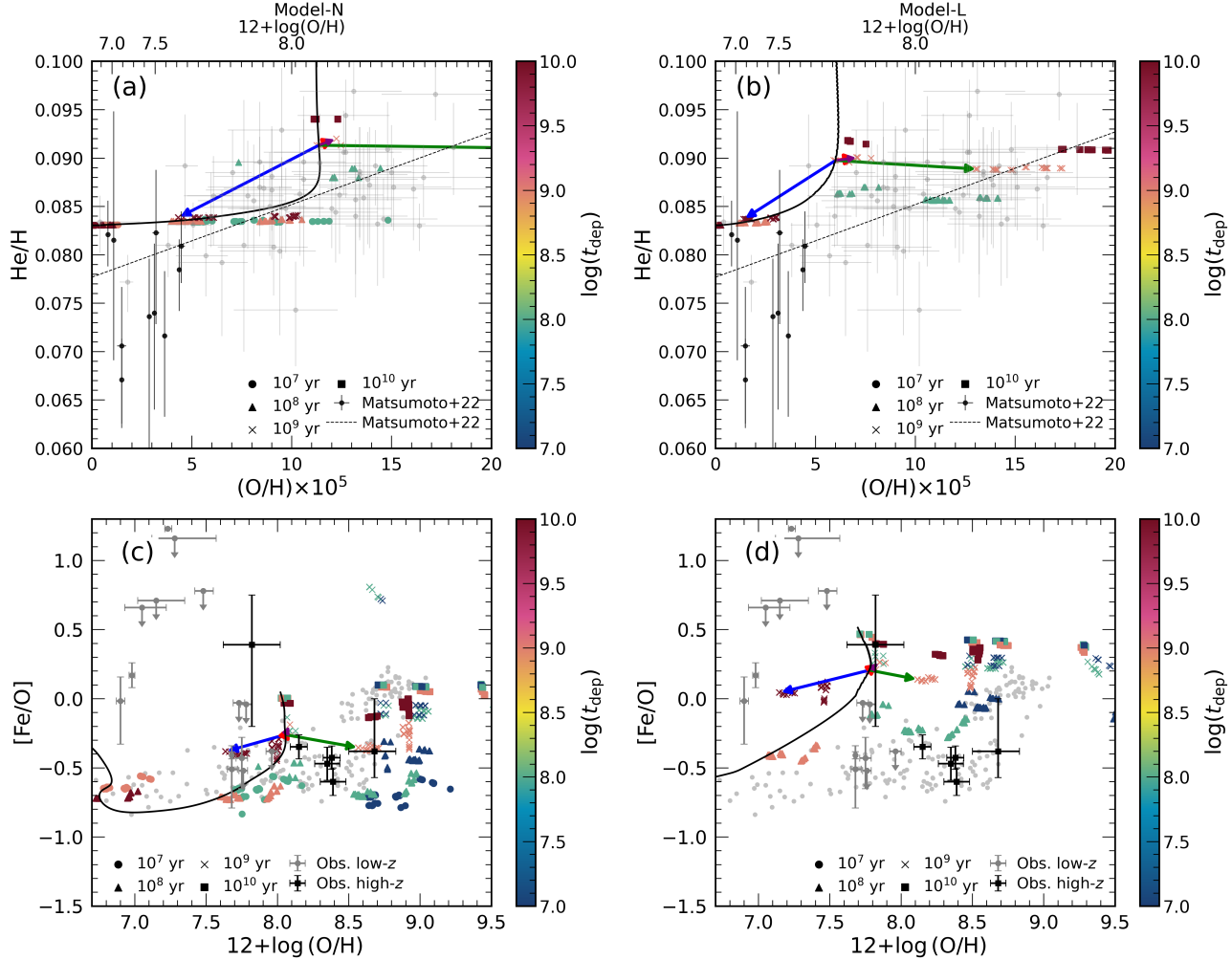


Figure 2. *Panel (a):* Evolution of He/H with metallicity in our Model-N. The different symbols indicate the chemical abundance of the galaxies at different ages. The color bar indicates t_{dep} . Black and gray points are the results of Matsumoto et al. (2022) and Hsyu et al. (2020), respectively. The black dashed line is the best linear fit to the observed data from Matsumoto et al. (2022). The black line represents the evolutionary track for the case of $(t_{\text{dep}}[\text{yr}], t_{\text{in}}[\text{yr}], f_o, f_{\text{inf}}) = (10^9, 10^{10}, 10, 0.01)$. The blue, red, green, and purple arrows indicate how the point on the track at 10^9 yr moves when the parameters are changed to $t_{\text{dep}} = 10^{10}$ yr, $t_{\text{in}} = 10^9$ yr, $f_o = 1$, and $f_{\text{inf}} = 0.1$, respectively. *Panel (b):* The same figure as panel (a) is plotted using the yields of Limongi & Chieffi (2018) (Model-L). *Panel (c):* The evolution of Fe/O with metallicity. Data points with black error bars show the chemical abundance of high- z galaxies (Steidel et al. 2016; Cullen et al. 2021; Kashino et al. 2022; Harikane et al. 2020; Nakane et al. 2024), while those with gray error bars represent low- z galaxies (Izotov et al. 2018b; Kojima et al. 2020, 2021; Isobe et al. 2022), and those with gray scatter represent MW stars (Amarsi et al. 2019). Galaxies with high Fe/O at low metallicity, which is particularly interesting for this study, are shown in black solid points. *Panel (d):* The same figure as panel (b) is plotted using the yields of Limongi & Chieffi (2018).

ters. This indicates that the results in Fig. 1 show that changing f_o and f_{inf} within the current parameter range only leads to variations within $\Delta((O/H) \times 10^5) = 5$.

In panel (c), our model illustrates that galaxies with a $12 + \log(O/H) \sim 7.0$ have a lower Fe/O ratio compared to what is observed. This difference is primarily attributed to the central role of CCSNe in the chemical evolution of these young galaxies in our model. Initially ($\sim 10^7$ years), a high Fe/O ratio is observed due to metal

enrichment by Pop III stars (as detailed in Appendix B), but this ratio is diminished over a period of approximately $10^{7.3}$ years by enrichment of α elements from conventional CCSNe. Additionally, our results indicate that galaxies around 1 Gyr old can exhibit relatively high Fe/O ratios ($[Fe/O] \sim -0.1$). Having higher Fe/O with lower star formation efficiency is also consistent with Vincenzo et al. (2014). Although EMPGs also display high Fe/O ratios, they possess a greater gas fraction

compared to those of the modeled galaxies. This divergence is likely due to more pronounced iron enrichment from SNIa in our galaxy sample, which is facilitated by their lower gas fractions. To observe $[\text{Fe}/\text{O}] \sim 0$ with $12 + \log(\text{O}/\text{H}) < 7.5$, it may be necessary to use SN yields from PISNe or bright HNe before $[\text{Fe}/\text{O}]$ decreases due to regular CCSNe (Isobe et al. 2022; Nakane et al. 2024). Alternatively, a top-light IMF may need to be employed (Yan et al. 2020; Mucciarelli et al. 2021). As shown in Appendix B, relatively low-mass CCSNe release high Fe/O ratios ($[\text{Fe}/\text{O}] \sim 0$). The trend of the black line and arrows for $[\text{Fe}/\text{O}]$ is also the same as in panel (a).

Panel (d), in contrast to panel (c), shows a galaxy with an age of 10^9 yr with $[\text{Fe}/\text{O}] \sim 0.0$ and $12 + \log(\text{O}/\text{H}) < 7.5$, this chemical abundance close to the observed galaxies. From the blue arrow, it can be seen that there is a parameter set with $(t_{\text{dep}}, t_{\text{in}}) = (10^{10}, 10^{10})$, and it appears that the longer t_{dep} , the lower the metallicity ($12 + \log(\text{O}/\text{H}) < 7.5$) and the higher the Fe/O ($[\text{Fe}/\text{O}] \sim 0.0$).

In summary, the use of Nomoto et al. (2013) yields (Model-N) in our models successfully replicates the observed galactic chemical properties for certain parameters. However, it falls short of accurately matching other aspects, such as the gas fraction, when compared to observations. In contrast, the application of Limongi & Chieffi (2018) yields appears to align more closely with observational data, offering a more consistent representation of the chemical evolution in galaxies.

3.2. Enrichment by Supermassive Stars

As seen in Figs. 1 and 2, it is difficult to achieve a high He/H ($\text{He}/\text{H} > 0.1$) like that of Yanagisawa et al. (2024) with low metallicity ($\text{O}/\text{H} \times 10^5 < 5$) in our standard model, even when using Limongi yield (Model-L), which considers stellar rotation. Therefore, in the following we also present the results of models which assumes that Pop III stars are SMS and using an intermittent star formation model.

Figure 3 shows the time evolution of O/H (panel (a)) and He/H (panel (b)) for models using SMS yield and for a star formation model with intermittent star formation. The age at which gas accretion begins is set to 0. The line types and models are as follows: Model-N_{int} (black solid), Model-N (gray dashed), Model-N&N-10% (blue solid), Model-N&N-10%-DC (dark blue dashed), Model-N&N-CO (red solid), and Model-N&N-CO-DC (dark red-dashed). The parameters were set as $t_{\text{dep}} = 10^9$ yr, $t_{\text{in}} = 10^9$ yr, $f_{\text{o}} = 10$, and $f_{\text{in}} = 0$.

In panel (a), Model-N shows an increase in O/H earlier, starting from $10^{6.6}$ yrs, compared to the other mod-

els. This is because star formation in the other models is intermittent, and since they do not form stars until the cumulative SFR exceeds the threshold, the first stars form later. In the case of Model-N&N-CO, $\text{O}/\text{H} \times 10^5$ reaches ~ 19 at $10^{7.5}$ yrs. This is due to the reduction in gas mass by outflow, mixing with oxygen released by SMS, after which O/H decreases due to primordial gas accretion. The lower O/H in Model-N&N-CO-DC compared to Model-N&N-CO at $10^{7.5}$ yrs is because SMS undergoes a direct collapse, resulting in no energy release and no reduction in gas mass due to outflow. Additionally, the lower O/H in Model-N&N-10% compared to Model-N&N-CO is because the ejected gas in this model is only 10% of the total mass of SMS, whereas everything up to the CO core is ejected in Model-N&N-CO.

Similar to Model-N&N-CO, Model-N_{int} also shows a higher O/H at $10^{7.5}$ yrs due to stronger outflow compared to Model-N, followed by a decrease due to primordial gas accretion. After $10^{8.3}$ yrs, all models follow a similar evolution. After 10^8 yrs, O/H increases due to oxygen enrichment and the increasing gas fraction as much of the gas is converted into stars. As the gas fraction decreases, the chemical abundance increasingly resembles the ejecta from AGB stars. For details on the abundance of the ejecta, see Appendix B).

Here, the gas fraction

$$\zeta_{\text{gas}} = M_{\text{gas}} / (M_{\text{gas}} + M_{\star}), \quad (1)$$

where M_{gas} is the gas mass and M_{\star} is the stellar mass in the box, is above 0.9 for all models until 10^7 yrs, 0.8 at 10^8 yrs, 0.45 at 10^9 yrs, and 0.04 at 10^{10} yrs.

From the He/H in the panel (b), it can be seen that Model-N&N-CO reaches $\text{He}/\text{H} = 0.12$ at $10^{7.5}$ yrs. This is due to the impact of outflow, similar to O/H. Although He/H would be expected to approach the primordial He abundance due to the accretion of primordial gas, no such decrease is observed because enrichment from SMS and low-metallicity stars continues even during gas accretion. Model-N&N-10% shows a lower He/H of 0.087 compared to Model-N&N-CO because the ejecta from the former has a lower He/H than the latter. Model-N&N-CO-DC shows that when outflow is not sufficiently effective, the primordial gas within the model results in lower He/H (~ 0.086). Additionally, Model-N_{int} reaches a higher He/H than Model-N at $10^{7.6}$ yrs due to strong outflow. Model-N&N-10%-DC does not differ much from Model-N. After this, He/H increases in all models due to contributions from AGB stars and other sources.

Fig. 4 shows the relation between $(\text{O}/\text{H}) \times 10^5$ and He/H, based on Fig. 3. The line types are the same

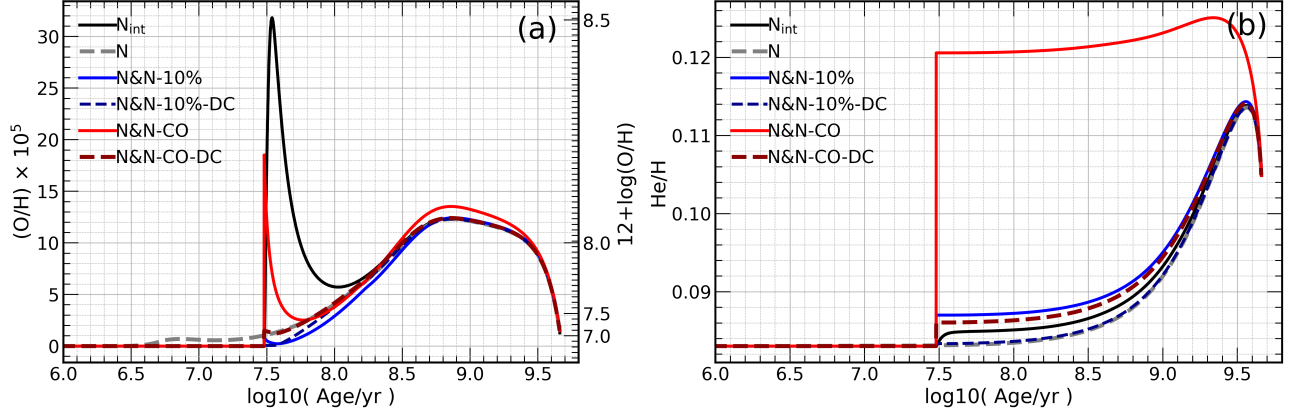


Figure 3. *Panel (a):* Time evolution of $O/H \times 10^5$. The age at which gas accretion begins is set to 0. The Model- N_{int} is shown with a black solid line, Model- N with a gray dashed line, Model- $N\&N-10\%$ with a blue solid line, Model- $N\&N-10\%-DC$ with a dark blue dashed line, Model- $N\&N-CO$ with a red solid line, and Model- $N\&N-CO-DC$ with a dark red-dashed line, respectively. Here, $t_{\text{dep}} = 10^9$ yr, $t_{\text{in}} = 10^9$ yr, $f_o = 10$, and $f_{\text{in}} = 0$ are used. *Panel (b):* Time evolution of He/H . The lines correspond to those in *panel (a)*.

as in Fig. 3. Data points with gray error bars show the observed galaxies by Hsyu et al. (2020); Matsumoto et al. (2022); Yanagisawa et al. (2024). Since EMPGs have abundant gas, each line plots the gas fraction up to 10%.

In the case of Model- $N\&N-CO$ (red line), He/H is the highest in the range of $O/H \times 10^5 < 20$. This is because the ratio of He enrichment to O enrichment from the SMS is higher compared to Model- N , resulting in a steeper evolution over time compared to the gray dashed line. Subsequently, both the inflow of primordial gas and the chemical enrichment by SMS and low-metallicity star clusters occur, keeping He/H high while the metallicity remains low. In the absence of chemical enrichment and with only the inflow of primordial gas, both O/H and He/H decrease towards the primordial He/H abundance ratio at $O/H \times 10^5 = 0$, i.e., to lower O/H without significantly changing He/H , as seen in the red line. The point where the gas mass reaches its maximum due to primordial gas accretion corresponds to the minimum O/H . As the gas fraction decreases, chemical evolution progresses, moving toward the upper right of the figure.

The Model- $N\&N-CO-DC$ (dark red dashed line) follows a similar chemical enrichment of Model- $N\&N-CO$ from $O/H \times 10^5 = 0$ to $O/H \times 10^5 < 1.5$. However, due to the lack of outflow, there is a larger amount of primordial gas within the halo compared to Model- $N\&N-CO$ (red line), and chemical enrichment by SMS stops at low abundance. Subsequently, O/H decreases to about 0.1 due to primordial gas accretion, but both O/H and He/H increase due to metal enrichment, with O/H peaking at $10^{8.8}$ yrs and He/H peaking at $10^{9.6}$ yrs due to

primordial gas accretion. This trend can be observed in all colored lines.

The Model- N_{int} (black line) shares the same star formation history as the Model- $N\&N$ series. Due to enrichment from Pop III stars, the metallicity reaches a high level with $O/H \times 10^5 > 20$. After this, gas accretion lowers the metallicity to around $O/H \times 10^5 \sim 6$. Following this, similar to other models, contributions from AGB stars and other sources increase both O/H and He/H , eventually depleting the gas.

4. DISCUSSION

4.1. Impact of SMS and intermittent star formation model

Metal enrichment by SMS is also being considered as a solution to the N/O abundance. The mass range of M_{SMS} used in Fig. 4 falls within the range that reproduces the N/O ratios observed in high- z galaxies by JWST, as identified by Nandal et al. (2024), and appears to be effective in achieving high He/H at young ages with $O/H \times 10^5 < 20$.

Additionally, Kobayashi & Ferrara (2024) pointed out that in the case of an intermittent star formation history, a high N/O can be achieved at young ages using a one-zone model. In our model, the intermittent case shows a higher He/H at $O/H \times 10^5 \sim 6$ compared to the continuous star formation model using the same yield model. This suggests that an intermittent star formation history is important for the chemical composition ratios of high- z galaxies, as shown by cosmological zoom-in hydrodynamic simulations (Yajima et al. 2017; Arata et al. 2019, 2020).

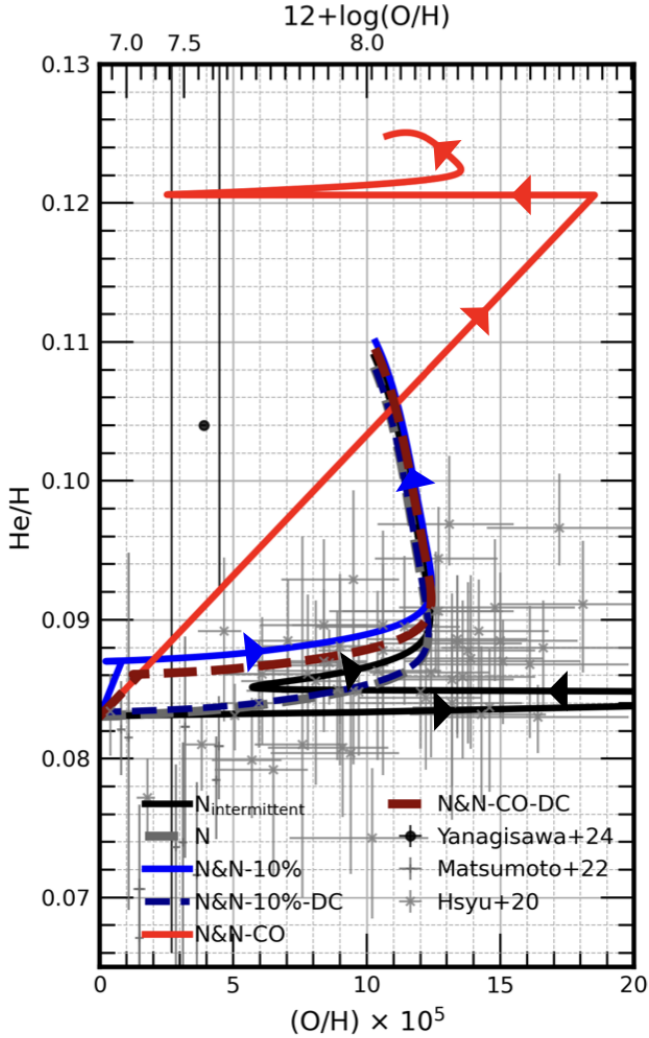


Figure 4. The same as Fig. 1, but using the SMS yield of Nandal et al. (2024) (Model-N&N series). Each line represents a plot from $\zeta_{\text{gas}} = 1$ to $\zeta_{\text{gas}} = 0.1$ with small arrows indicating the direction of time evolution. The line types and the parameters are the same as in Fig. 3. Data points with gray error bars show the observed galaxies’ He/H and $O/H \times 10^5$ (Hsyu et al. 2020; Matsumoto et al. 2022; Yanagisawa et al. 2024).

In Fig. 4, we demonstrated that SMS and an intermittent star formation history, both of which are considered effective in reproducing galaxies with high N/O ratios at high redshifts, are also effective in reproducing galaxies with low metallicity and high He/H ratios. In Fig. 5, we plot the evolution in $[N/O]$ vs. $12 + \log(O/H)$ using the same yield set, star formation history, and line types as in Fig. 4. We can see that SMS can raise N/O to $[N/O] = 1.8$ (in Model-N&N-10%) and 1.5 (in Model-

N&N-CO), while still maintaining a low metallicity of $12 + \log(O/H) < 8.3$. Subsequently, due to regular CC-SNe, the N/O ratio decreases and converges with Model-N at around $12 + \log(O/H) = 8.05$ and $[N/O] = -0.3$. Our model also appears to reproduce the high N/O ratios observed in high- z galaxies through the contribution of SMS.

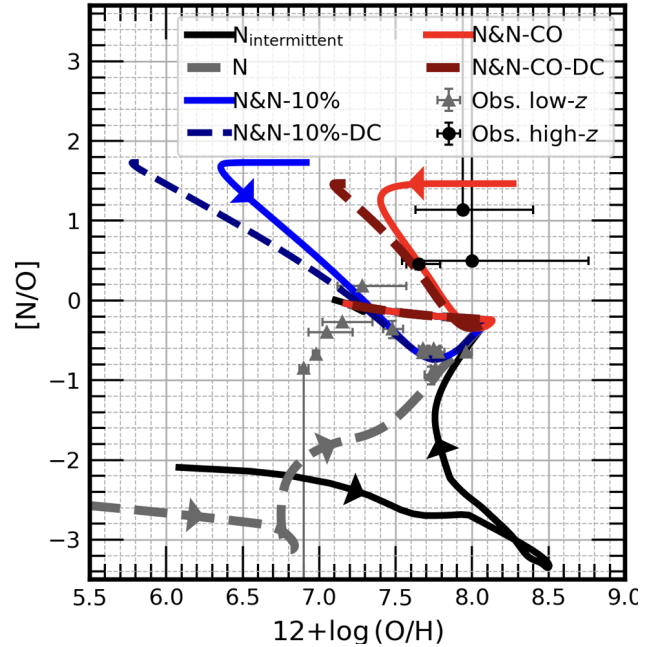


Figure 5. The evolutionary track of $[N/O]$ and $12 + \log(O/H)$ using the same yield set, star formation history, and parameters as those used in Fig. 4. However, here we plot from $\zeta_{\text{gas}} = 1$ to $\zeta_{\text{gas}} = 0$ with small arrows indicating the direction of time evolution. Data points with gray error bars show the observed galaxies by Izotov et al. (2018a); Kojima et al. (2021); Isoabe et al. (2022, 2023); Yanagisawa et al. (2024).

4.2. How to Estimate the Primordial He/H Ratio

The insights drawn from Fig. 2 suggest that, to determine the primordial He/H from observational data, it is necessary to accurately measure the He/H ratio of galaxies before the gas fraction decreases to 0.6. As indicated by the black line in Fig. 2, the He/H ratio increases sharply as the gas fraction decreases to 0.6. Furthermore, in the current model, the $O/H \times 10^5$ does not increase significantly because CCSNe do not effectively release oxygen at that age. By excluding galaxies with low gas fractions ($\zeta_{\text{gas}} < 0.6$) that exhibit high He/H ratios (> 0.09), it may be possible to obtain a more robust relation to estimate primordial He abundance.

To handle more realistic gas inflows, star formation histories, and outflows beyond the one-zone model, it is

essential to perform simulations of EMPGs and dwarf galaxies with high mass resolution. However, conducting such simulations remains a significant challenge for future research. In particular, such a simulation may answer the question of whether EMPGs are local analogs of the first galaxies. Additionally, it is anticipated that these simulations will extend to normal dwarf galaxies, providing an opportunity to validate the t_{dep} dependence of the He/H–O/H relationship, as derived from our one-zone model results.

An obvious future task is to expand the dataset of He/H and O/H observations in galaxies with low metallicity and compare the fitting curves across different specific SFRs. This requires deep spectroscopic observations of many dwarf galaxies, including EMPGs. Information on the He/H–O/H relation of high- z galaxies, as observed by JWST, is also important and will be the subject of future work.

5. SUMMARY

We investigate the chemical evolution of EMPGs employing the one-zone box model with different yield models. The findings from our model indicate that galaxies with long gas-depletion timescales achieve high He/H at low metallicity, similar to the observed data, when using the Limongi & Chieffi (2018) yield (Model-L) which includes metal enrichment from the WR star. The Model-L also reproduces high Fe/O ($[\text{Fe}/\text{H}] \sim 0.0$) at low metallicity ($12 + \log(\text{O}/\text{H}) < 7.5$) with long gas-depletion timescales, comparable to the observed EMPGs, while Model-N has difficulty in achieving $[\text{Fe}/\text{O}] > 0.1$.

Using SMS yields (Model-N&N series) can further help explain galaxies with metallicities of $(\text{O}/\text{H}) \times 10^5 < 20$ and $\text{He}/\text{H} > 0.085$ at young ages ($< 10^8$ yrs). Additionally, our Model-N&N-CO can achieve $\text{He}/\text{H} > 0.12$, comparable to the high- z galaxies found by JWST.

These SMS yield models also show high $[\text{N}/\text{O}] > 0.3$, as observed by JWST in high- z galaxies.

Finally, we discuss future prospects. To more accurately reproduce the observed chemical abundance in young, low-metallicity galaxies such as EMPGs and first galaxies, a sufficiently high-resolution cosmological hydrodynamic simulation capable of handling realistic baryon cycles down to $z = 0$ needs to be performed. These simulations will focus on simulating EMPGs and dwarf galaxies, capturing starbursts and the impact of different yield models, such as those of rotating massive stars. Additionally, expanding the dataset of He/H and O/H observations in low-metallicity galaxies will be crucial. This entails deep spectroscopic observations of a wide array of dwarf galaxies, including EMPGs, with different specific SFR. The emerging data from the JWST on high- z galaxies will also play a pivotal role in refining our understanding of the He/H–O/H relationship and its dependence on specific star formation rates. These steps will significantly contribute to confirming whether EMPGs are indeed local analogs of the first galaxies and provide a more comprehensive understanding of their chemical evolution.

6. ACKNOWLEDGMENTS

Numerical computations were carried out on the Cray XC50 at the Center for Computational Astrophysics, National Astronomical Observatory of Japan, and SQUID at the Cybermedia Center, Osaka University, as part of the HPCI system Research Project (hp230089, hp240141). This work is supported in part by the MEXT/JSPS KAKENHI grant numbers 20H00180, 22K21349, 24H00002, 24H00241 (K.N.), 22KJ0157, 20K14532, 21H04499, 21K03614, 22H01259 (Y.H.), 21J20785 (Y.I.). This work was supported by JST SPRING, grant number JPMJSP2138 (K.F.). K.N. acknowledges the travel support from the Kavli IPMU, World Premier Research Center Initiative (WPI), where part of this work was conducted.

APPENDIX

A. ONE-ZONE BOX MODEL

In this section, we present the governing equations and parameters of our one-zone model for the chemical evolution of galaxies, which assumes that the cold ISM is uniformly enriched by metals. Treatment of the chemical enrichment of ISM in this approximation is well established (e.g. Tinsley 1980; Matteucci & Greggio 1986; Matteucci & Franco 1989; Prantzos et al. 1993; Timmes et al. 1995; Chiappini et al. 1997; Matteucci 2001; Kobayashi et al. 2006; Suzuki & Maeda 2018; Kobayashi et al. 2020; Kobayashi & Ferrara 2024). In this study, we mainly follow Kobayashi & Taylor (2023).

The time evolution of the mass fraction Z_i of the i th component (H, He, metals) in the gas phase of a one-zone box can be written as follows:

$$\frac{d(Z_i(t)f_{\text{gas}}(t))}{dt} = Z_{i,\text{in}}(t)\dot{R}_{\text{in}}(t) + \dot{E}_{\text{eje},i}(t) - Z_i(t)\psi(t) - Z_i(t)\dot{R}_{\text{out}}(t), \quad (\text{A1})$$

where each term on the right-hand side corresponds to gas inflow rate, element ejection rate into ISM from SNe, gas mass incorporated by stars during star formation, and gas outflow rate from the galaxy by SNe. Eq. A1 is normalized by the total accreted gas mass in a one-zone box model (see Eq. A2). Here, f_{gas} is the gas fraction or the total gas mass in the system of a unit mass as a function of time, $Z_{i,\text{in}}$ is the mass ratio of the i th component in the accreted gas, \dot{R}_{in} is the gas accretion rate, ψ is the star formation rate, \dot{R}_{out} is the mass outflow rate, and $\dot{E}_{\text{eje},i}$ is the mass ejection rate into the ISM by the SNe. In $\dot{E}_{\text{eje},i}$, the total yield is obtained by adding the net yield of each element newly produced by the star to the abundance of each element that the star has at the time of its formation. The net yields are based on the values calculated by Nomoto et al. (2013); Limongi & Chieffi (2018); Nandal et al. (2024). We explore the varying metallicities of accreted gas with $f_{\text{inf}} = Z_{i,\text{in}}/Z_i = 0, 0.01, 0.1, 1.0$.

The gas mass accretion rate is assumed as

$$\dot{R}_{\text{in}}(t) = \frac{1}{t_{\text{in}}} \exp\left(-\frac{t}{t_{\text{in}}}\right), \quad (\text{A2})$$

where t_{in} is the gas accretion timescale. The numerator in the first term on the right-hand-side is unity, as it is normalized by the total accreted gas mass.

The SFR can be written as

$$\psi(t) = \frac{f_{\text{gas}}(t)}{t_{\text{dep}}}, \quad (\text{A3})$$

where t_{dep} is the star formation timescale.

The outflow rate is usually taken as $\dot{R}_{\text{out}} = f_o\psi$. However, we use SN energy directly, and calculate the outflow rate as follows:

$$\dot{R}_{\text{out}}(t) = \dot{e}_{\text{SN}}(t) \frac{100 M_{\odot}}{10^{51} \text{ erg}} \times f_o, \quad (\text{A4})$$

where the energy injection rate by SN, $\dot{e}_{\text{SN}}(t)$, is computed as

$$\dot{e}_{\text{SN}}(t) = \int_0^t \dot{E}_{\text{CCSN,SNIa}}(t - t_{\text{form}}) \psi(t_{\text{form}}) dt_{\text{form}}. \quad (\text{A5})$$

The term $100 M_{\odot}/10^{51}$ erg in Eq. A4 is based on the assumption that the energy output from a star cluster of $100 M_{\odot}$ is 10^{51} ergs. Here, $\dot{E}_{\text{CCSN,SNIa}}(t - t_{\text{form}})$ is the energy emitted per unit time per unit mass by CCSNe and SN Ia from individual star clusters, which depends on the SN event rate and IMF. Therefore, $\dot{E}_{\text{CCSN,SNIa}}$ is dependent on the current time t and the star cluster's formation time t_{form} . Since $\dot{E}_{\text{CCSN,SNIa}}(t - t_{\text{form}})$ is the energy release per unit mass, we multiply by ψ to use the mass at the formation time.

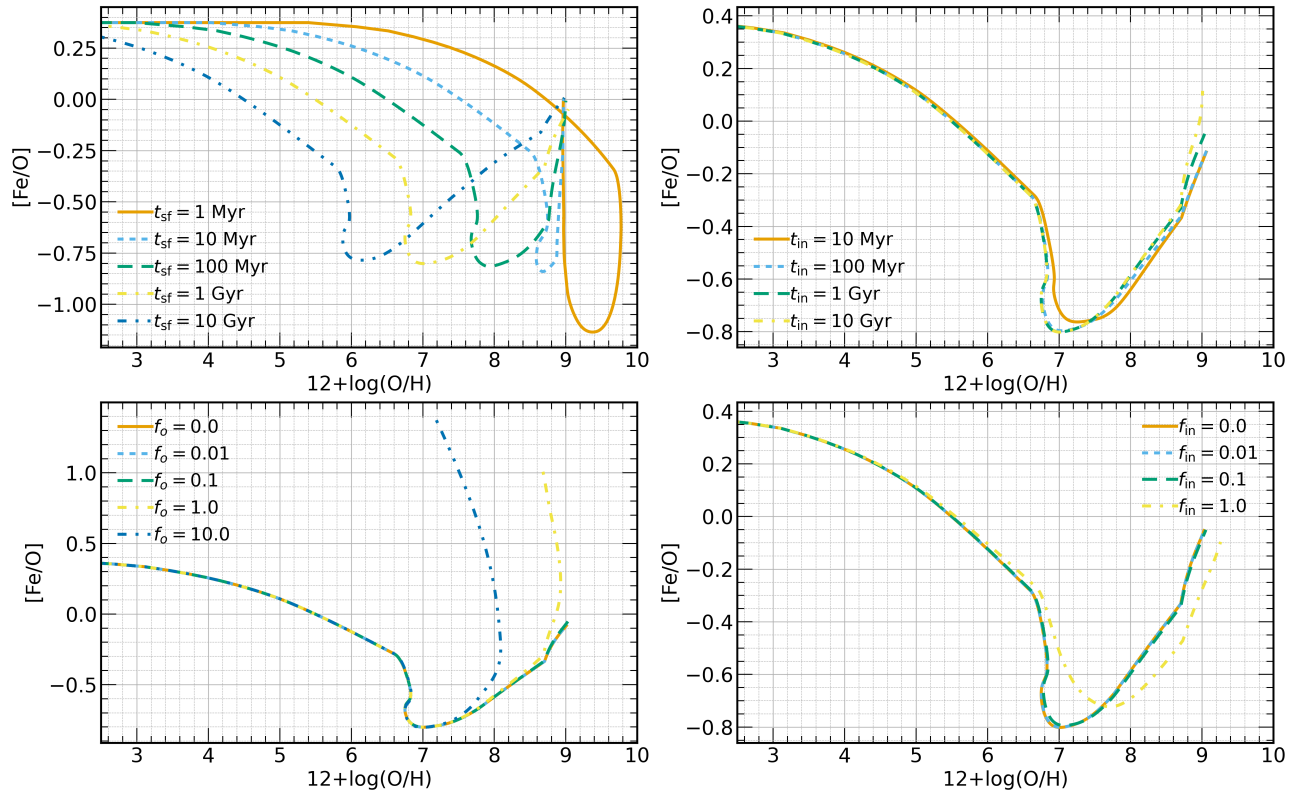
Similarly to Equation A5, the element ejection rate due to SN can be written as

$$\dot{E}_{\text{eje},i}(t) = \int_0^t \psi(t_{\text{form}}) \dot{Y}_i(t - t_{\text{form}}) dt_{\text{form}}, \quad (\text{A6})$$

where $\dot{Y}_i(t - t_{\text{form}})$ represents the mass ejection rate per unit mass of the star cluster per unit time for i th elements, originating from the stellar cluster. Quantities $\dot{E}_{\text{CCSN,SNIa}}(t - t_{\text{form}})$ and $\dot{Y}_i(t - t_{\text{form}})$ were calculated using CELIB (Saitoh 2016, 2017).

To enhance understanding of the one-zone model calculation, we provide a comparison of fundamental outcomes from different yield models. Figure 6 shows the evolutionary track of the one-zone model calculation presented in Fig. 2(c,d). The top four panels show Model-N, and the bottom four panels show Model-L. Each of the four panels shows the variation in parameters t_{dep} , t_{in} , f_{in} , and f_o clockwise. The following parameters were chosen as fiducial values: $t_{\text{dep}} = 10^9$ yrs, $t_{\text{in}} = 10^9$ yrs, $f_{\text{in}} = 0.0$, and $f_o = 0.1$. The pathway of chemical evolution is influenced by the choice of yields, with t_{dep} playing a primary role. A larger value of f_o leads to an increase in the Fe/O due to SN Ia contributions, accentuating the impact of gas outflow and the most recent metal enrichment. The evolutionary tracks in the upper four panels begin with a high Fe/O ratio, approximately 0.35, a consequence of metal enrichment by PISN from Pop III stars. In the Limongi & Chieffi (2018) yield, on the other hand, metal enrichment by CCSNe is mainly contributed by the WR star, resulting in low Fe/O values at low metallicities in the one-zone model.

Model-N



Model-L

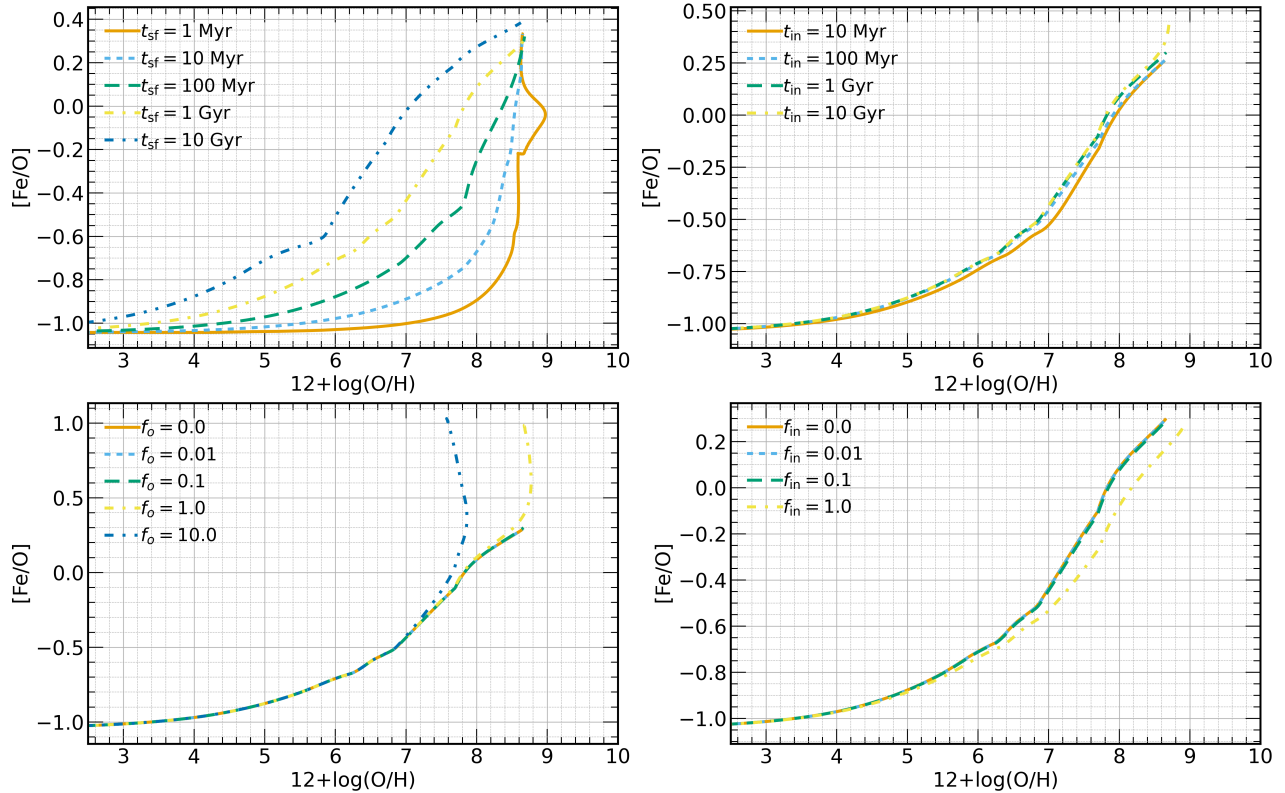


Figure 6. Chemical evolution track of Fe/O vs. O/H from our one-zone model. The top 4 panels are for Model-N (Nomoto et al. 2013), and the bottom 4 panels are for Model-L (Limongi & Chieffi 2018). Each of the four panels shows the variation in parameters t_{dep} , t_{in} , f_{in} , and f_{o} clockwise.

B. CELIB RESULT of O/H, He/H, and Fe/O

To help understand the results of different yield models, we present the time evolution of O/H (*panel (a), (b)*), He/H (*panel (c), (d)*), and Fe/O (*panel (e), (f)*) emitted from an instantaneous burst of a simple stellar population calculated using CELIB in Figure 7. In panel (*a*), (*b*), (*c*), and (*d*), the SMS yield for the case where 10% of the total mass is ejected for $M_{\text{SMS}} = 6127 M_{\odot}$ (Model-N&N-10%) is shown by a gray dashed line, and the SMS yield for the case where all outer layers up to the CO core are ejected for $M_{\text{SMS}} = 6127 M_{\odot}$ (Model-N&N-CO) is shown by a gray solid line. At $t = 10^{7.6}$ yr in panel (*e*) and (*f*), Fe release by SNIa begins to occur, increasing Fe/O in both panels. The high Fe/O ($[\text{Fe}/\text{O}] > 0$) at $\sim 10^{6.5}$ yr for $Z = 10^{-7}$ (Pop III) case in the panel (*e*) is due to metal enrichment by PISN. Additionally, in panel (*f*), a high $[\text{Fe}/\text{O}]$ ($[\text{Fe}/\text{O}] > 0$) does not appear because the massive star collapses directly to BH.

REFERENCES

- Amarsi, A. M., Nissen, P. E., & Skúladóttir, Á. 2019, *A&A*, 630, A104, doi: [10.1051/0004-6361/201936265](https://doi.org/10.1051/0004-6361/201936265)
- Arata, S., Yajima, H., Nagamine, K., Abe, M., & Khochfar, S. 2020, *MNRAS*, 498, 5541, doi: [10.1093/mnras/staa2809](https://doi.org/10.1093/mnras/staa2809)
- Arata, S., Yajima, H., Nagamine, K., Li, Y., & Khochfar, S. 2019, *MNRAS*, 488, 2629, doi: [10.1093/mnras/stz1887](https://doi.org/10.1093/mnras/stz1887)
- Arrabal Haro, P., Dickinson, M., Finkelstein, S. L., et al. 2023a, *ApJL*, 951, L22, doi: [10.3847/2041-8213/acdd54](https://doi.org/10.3847/2041-8213/acdd54)
- . 2023b, *Nature*, 622, 707, doi: [10.1038/s41586-023-06521-7](https://doi.org/10.1038/s41586-023-06521-7)
- Asplund, M., Amarsi, A. M., & Grevesse, N. 2021, *A&A*, 653, A141, doi: [10.1051/0004-6361/202140445](https://doi.org/10.1051/0004-6361/202140445)
- Barkat, Z., Rakavy, G., & Sack, N. 1967, *PhRvL*, 18, 379, doi: [10.1103/PhysRevLett.18.379](https://doi.org/10.1103/PhysRevLett.18.379)
- Bunker, A. J., Saxena, A., Cameron, A. J., et al. 2023, *A&A*, 677, A88, doi: [10.1051/0004-6361/202346159](https://doi.org/10.1051/0004-6361/202346159)
- Cameron, A. J., Katz, H., Rey, M. P., & Saxena, A. 2023, *MNRAS*, 523, 3516, doi: [10.1093/mnras/stad1579](https://doi.org/10.1093/mnras/stad1579)
- Campbell, S. W., & Lattanzio, J. C. 2008, *A&A*, 490, 769, doi: [10.1051/0004-6361:200809597](https://doi.org/10.1051/0004-6361:200809597)
- Chabrier, G. 2003, *PASP*, 115, 763, doi: [10.1086/376392](https://doi.org/10.1086/376392)
- Charbonnel, C., Schaerer, D., Prantzos, N., et al. 2023, *A&A*, 673, L7, doi: [10.1051/0004-6361/202346410](https://doi.org/10.1051/0004-6361/202346410)
- Chiappini, C., Matteucci, F., & Gratton, R. 1997, *ApJ*, 477, 765, doi: [10.1086/303726](https://doi.org/10.1086/303726)
- Chon, S., Hosokawa, T., Omukai, K., & Schneider, R. 2023, arXiv e-prints, arXiv:2312.13339, doi: [10.48550/arXiv.2312.13339](https://doi.org/10.48550/arXiv.2312.13339)
- Chon, S., Omukai, K., & Schneider, R. 2021, *MNRAS*, 508, 4175, doi: [10.1093/mnras/stab2497](https://doi.org/10.1093/mnras/stab2497)
- Chon, S., Ono, H., Omukai, K., & Schneider, R. 2022, *MNRAS*, 514, 4639, doi: [10.1093/mnras/stac1549](https://doi.org/10.1093/mnras/stac1549)
- Cullen, F., Shapley, A. E., McLure, R. J., et al. 2021, *MNRAS*, 505, 903, doi: [10.1093/mnras/stab1340](https://doi.org/10.1093/mnras/stab1340)
- Curti, M., D'Eugenio, F., Carniani, S., et al. 2023a, *MNRAS*, 518, 425, doi: [10.1093/mnras/stac2737](https://doi.org/10.1093/mnras/stac2737)
- Curti, M., Maiolino, R., Curtis-Lake, E., et al. 2023b, arXiv e-prints, arXiv:2304.08516, doi: [10.48550/arXiv.2304.08516](https://doi.org/10.48550/arXiv.2304.08516)
- Curtis-Lake, E., Carniani, S., Cameron, A., et al. 2023, *Nature Astronomy*, 7, 622, doi: [10.1038/s41550-023-01918-w](https://doi.org/10.1038/s41550-023-01918-w)
- Doherty, C. L., Gil-Pons, P., Lau, H. H. B., Lattanzio, J. C., & Siess, L. 2014, *MNRAS*, 437, 195, doi: [10.1093/mnras/stt1877](https://doi.org/10.1093/mnras/stt1877)
- Fukushima, K., Nagamine, K., & Shimizu, I. 2023, *MNRAS*, 525, 3760, doi: [10.1093/mnras/stad2526](https://doi.org/10.1093/mnras/stad2526)
- Gil-Pons, P., Doherty, C. L., Lau, H., et al. 2013, *A&A*, 557, A106, doi: [10.1051/0004-6361/201321127](https://doi.org/10.1051/0004-6361/201321127)
- Harikane, Y., Laporte, N., Ellis, R. S., & Matsuoka, Y. 2020, *ApJ*, 902, 117, doi: [10.3847/1538-4357/abb597](https://doi.org/10.3847/1538-4357/abb597)
- Harikane, Y., Nakajima, K., Ouchi, M., et al. 2024, *ApJ*, 960, 56, doi: [10.3847/1538-4357/ad0b7e](https://doi.org/10.3847/1538-4357/ad0b7e)
- Harikane, Y., Ouchi, M., Oguri, M., et al. 2023, *ApJS*, 265, 5, doi: [10.3847/1538-4365/acaaa9](https://doi.org/10.3847/1538-4365/acaaa9)
- Heger, A., & Woosley, S. E. 2002, *ApJ*, 567, 532, doi: [10.1086/338487](https://doi.org/10.1086/338487)
- Hsyu, T., Cooke, R. J., Prochaska, J. X., & Bolte, M. 2020, *ApJ*, 896, 77, doi: [10.3847/1538-4357/ab91af](https://doi.org/10.3847/1538-4357/ab91af)
- Isobe, Y., Ouchi, M., Suzuki, A., et al. 2022, *ApJ*, 925, 111, doi: [10.3847/1538-4357/ac3509](https://doi.org/10.3847/1538-4357/ac3509)
- Isobe, Y., Ouchi, M., Tominaga, N., et al. 2023, *ApJ*, 959, 100, doi: [10.3847/1538-4357/ad09be](https://doi.org/10.3847/1538-4357/ad09be)
- Izotov, Y. I., Thuan, T. X., Guseva, N. G., & Liss, S. E. 2018a, *MNRAS*, 473, 1956, doi: [10.1093/mnras/stx2478](https://doi.org/10.1093/mnras/stx2478)
- Izotov, Y. I., Worseck, G., Schaerer, D., et al. 2018b, *MNRAS*, 478, 4851, doi: [10.1093/mnras/sty1378](https://doi.org/10.1093/mnras/sty1378)
- Johnson, J. L., Dalla Vecchia, C., & Khochfar, S. 2013, *MNRAS*, 428, 1857, doi: [10.1093/mnras/sts011](https://doi.org/10.1093/mnras/sts011)
- Karakas, A. I. 2010, *MNRAS*, 403, 1413, doi: [10.1111/j.1365-2966.2009.16198.x](https://doi.org/10.1111/j.1365-2966.2009.16198.x)
- Kashino, D., Lilly, S. J., Renzini, A., et al. 2022, *ApJ*, 925, 82, doi: [10.3847/1538-4357/ac399e](https://doi.org/10.3847/1538-4357/ac399e)

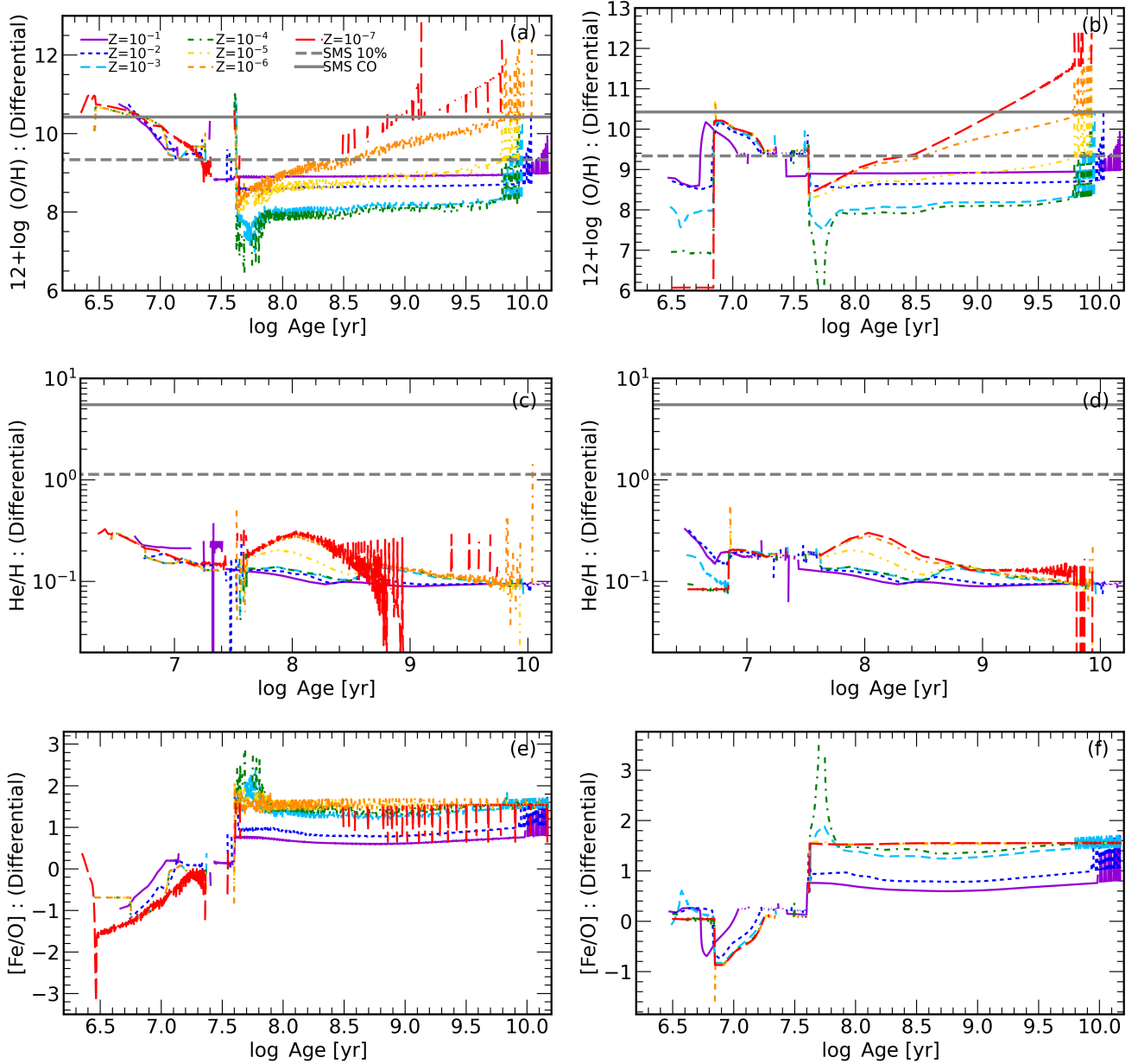


Figure 7. Differential output of ejecta's chemical abundance: O/H (panel (a), (b)), He/H (panel (c), (d)), and Fe/O (panel (e), (f)) from CELIB for an instantaneous burst of a simple stellar population. The left column is for Model-N, and the right column is for Model-L. The gray solid line shows the yield of SMS for the case where all outer layers above the CO core are ejected for $M_{\text{SMS}} = 6127 M_{\odot}$ (Model-N&N-CO), and the gray dashed line shows the SMS yield for the case where 10% of the total mass is ejected for $M_{\text{SMS}} = 6127 M_{\odot}$ (Model-N&N-10%).

Kimm, T., & Cen, R. 2014, ApJ, 788, 121,

doi: [10.1088/0004-637X/788/2/121](https://doi.org/10.1088/0004-637X/788/2/121)

Kobayashi, C., & Ferrara, A. 2024, ApJL, 962, L6,

doi: [10.3847/2041-8213/ad1de1](https://doi.org/10.3847/2041-8213/ad1de1)

Kobayashi, C., Karakas, A. I., & Lugaro, M. 2020, ApJ,

900, 179, doi: [10.3847/1538-4357/abae65](https://doi.org/10.3847/1538-4357/abae65)

Kobayashi, C., & Taylor, P. 2023, arXiv e-prints,

arXiv:2302.07255, doi: [10.48550/arXiv.2302.07255](https://doi.org/10.48550/arXiv.2302.07255)

Kobayashi, C., Umeda, H., Nomoto, K., Tominaga, N., &

Ohkubo, T. 2006, ApJ, 653, 1145, doi: [10.1086/508914](https://doi.org/10.1086/508914)

Kojima, T., Ouchi, M., Rauch, M., et al. 2020, ApJ, 898,

142, doi: [10.3847/1538-4357/aba047](https://doi.org/10.3847/1538-4357/aba047)

—. 2021, ApJ, 913, 22, doi: [10.3847/1538-4357/abec3d](https://doi.org/10.3847/1538-4357/abec3d)

Kumari, N., James, B. L., Irwin, M. J., Amorín, R., &

Pérez-Montero, E. 2018, MNRAS, 476, 3793,

doi: [10.1093/mnras/sty402](https://doi.org/10.1093/mnras/sty402)

- Limongi, M., & Chieffi, A. 2018, *ApJS*, 237, 13, doi: [10.3847/1538-4365/aacb24](https://doi.org/10.3847/1538-4365/aacb24)
- Maoz, D., & Mannucci, F. 2012, *PASA*, 29, 447, doi: [10.1071/AS11052](https://doi.org/10.1071/AS11052)
- Maoz, D., Mannucci, F., & Nelemans, G. 2014, *ARA&A*, 52, 107, doi: [10.1146/annurev-astro-082812-141031](https://doi.org/10.1146/annurev-astro-082812-141031)
- Matsumoto, A., Ouchi, M., Nakajima, K., et al. 2022, *ApJ*, 941, 167, doi: [10.3847/1538-4357/ac9ea1](https://doi.org/10.3847/1538-4357/ac9ea1)
- Matteucci, F. 2001, The chemical evolution of the Galaxy, Vol. 253, doi: [10.1007/978-94-010-0967-6](https://doi.org/10.1007/978-94-010-0967-6)
- Matteucci, F., & Francois, P. 1989, *MNRAS*, 239, 885, doi: [10.1093/mnras/239.3.885](https://doi.org/10.1093/mnras/239.3.885)
- Matteucci, F., & Greggio, L. 1986, *A&A*, 154, 279
- Mucciarelli, A., Massari, D., Minelli, A., et al. 2021, *Nature Astronomy*, 5, 1247, doi: [10.1038/s41550-021-01493-y](https://doi.org/10.1038/s41550-021-01493-y)
- Nakajima, K., Ouchi, M., Isobe, Y., et al. 2023, *ApJS*, 269, 33, doi: [10.3847/1538-4365/acd556](https://doi.org/10.3847/1538-4365/acd556)
- Nakane, M., Ouchi, M., Nakajima, K., et al. 2024, arXiv e-prints, arXiv:2407.14470, doi: [10.48550/arXiv.2407.14470](https://doi.org/10.48550/arXiv.2407.14470)
- Nandal, D., Regan, J. A., Woods, T. E., et al. 2024, *A&A*, 683, A156, doi: [10.1051/0004-6361/202348035](https://doi.org/10.1051/0004-6361/202348035)
- Nomoto, K., Kobayashi, C., & Tominaga, N. 2013, *ARA&A*, 51, 457, doi: [10.1146/annurev-astro-082812-140956](https://doi.org/10.1146/annurev-astro-082812-140956)
- Planck Collaboration, Ade, P. A. R., Aghanim, N., et al. 2016, *A&A*, 594, A13, doi: [10.1051/0004-6361/201525830](https://doi.org/10.1051/0004-6361/201525830)
- Prantzos, N., Casse, M., & Vangioni-Flam, E. 1993, *ApJ*, 403, 630, doi: [10.1086/172233](https://doi.org/10.1086/172233)
- Roberts-Borsani, G., Treu, T., Chen, W., et al. 2023, *Nature*, 618, 480, doi: [10.1038/s41586-023-05994-w](https://doi.org/10.1038/s41586-023-05994-w)
- Romano-Díaz, E., Shlosman, I., Choi, J.-H., & Sadoun, R. 2014, *ApJL*, 790, L32, doi: [10.1088/2041-8205/790/2/L32](https://doi.org/10.1088/2041-8205/790/2/L32)
- Saitoh, T. R. 2016, CELib: Software library for simulations of chemical evolution. <http://ascl.net/1612.016>
- . 2017, *AJ*, 153, 85, doi: [10.3847/1538-3881/153/2/85](https://doi.org/10.3847/1538-3881/153/2/85)
- Seitzzahl, I. R., Ciaraldi-Schoolmann, F., Röpke, F. K., et al. 2013, *MNRAS*, 429, 1156, doi: [10.1093/mnras/sts402](https://doi.org/10.1093/mnras/sts402)
- Senchyna, P., Plat, A., Stark, D. P., & Rudie, G. C. 2023, arXiv e-prints, arXiv:2303.04179, doi: [10.48550/arXiv.2303.04179](https://doi.org/10.48550/arXiv.2303.04179)
- Steidel, C. C., Strom, A. L., Pettini, M., et al. 2016, *ApJ*, 826, 159, doi: [10.3847/0004-637X/826/2/159](https://doi.org/10.3847/0004-637X/826/2/159)
- Susa, H., Hasegawa, K., & Tominaga, N. 2014, *ApJ*, 792, 32, doi: [10.1088/0004-637X/792/1/32](https://doi.org/10.1088/0004-637X/792/1/32)
- Suzuki, A., & Maeda, K. 2018, *ApJ*, 852, 101, doi: [10.3847/1538-4357/aaa024](https://doi.org/10.3847/1538-4357/aaa024)
- Timmes, F. X., Woosley, S. E., & Weaver, T. A. 1995, *ApJS*, 98, 617, doi: [10.1086/192172](https://doi.org/10.1086/192172)
- Tinsley, B. M. 1980, *FCPh*, 5, 287
- Totani, T., Morokuma, T., Oda, T., Doi, M., & Yasuda, N. 2008, *PASJ*, 60, 1327, doi: [10.1093/pasj/60.6.1327](https://doi.org/10.1093/pasj/60.6.1327)
- Umeda, H., & Nomoto, K. 2002, *ApJ*, 565, 385, doi: [10.1086/323946](https://doi.org/10.1086/323946)
- Vanzella, E., Loiacono, F., Bergamini, P., et al. 2023, *A&A*, 678, A173, doi: [10.1051/0004-6361/202346981](https://doi.org/10.1051/0004-6361/202346981)
- Ventura, P., Di Criscienzo, M., Carini, R., & D'Antona, F. 2013, *MNRAS*, 431, 3642, doi: [10.1093/mnras/stt444](https://doi.org/10.1093/mnras/stt444)
- Vincenzo, F., Matteucci, F., Vattakunnel, S., & Lanfranchi, G. A. 2014, *MNRAS*, 441, 2815, doi: [10.1093/mnras/stu710](https://doi.org/10.1093/mnras/stu710)
- Vincenzo, F., Miglio, A., Kobayashi, C., Mackereth, J. T., & Montalbán, J. 2019, *A&A*, 630, A125, doi: [10.1051/0004-6361/201935886](https://doi.org/10.1051/0004-6361/201935886)
- Watanabe, K., Ouchi, M., Nakajima, K., et al. 2023, arXiv e-prints, arXiv:2305.02078, doi: [10.48550/arXiv.2305.02078](https://doi.org/10.48550/arXiv.2305.02078)
- Williams, H., Kelly, P. L., Chen, W., et al. 2023, *Science*, 380, 416, doi: [10.1126/science.adf5307](https://doi.org/10.1126/science.adf5307)
- Wise, J. H., Turk, M. J., Norman, M. L., & Abel, T. 2012, *ApJ*, 745, 50, doi: [10.1088/0004-637X/745/1/50](https://doi.org/10.1088/0004-637X/745/1/50)
- Yajima, H., Abe, M., Fukushima, H., et al. 2023, *MNRAS*, 525, 4832, doi: [10.1093/mnras/stad2497](https://doi.org/10.1093/mnras/stad2497)
- Yajima, H., Nagamine, K., Zhu, Q., Khochfar, S., & Dalla Vecchia, C. 2017, *ApJ*, 846, 30, doi: [10.3847/1538-4357/aa82b5](https://doi.org/10.3847/1538-4357/aa82b5)
- Yan, Z., Jerabkova, T., & Kroupa, P. 2020, *A&A*, 637, A68, doi: [10.1051/0004-6361/202037567](https://doi.org/10.1051/0004-6361/202037567)
- Yanagisawa, H., Ouchi, M., Watanabe, K., et al. 2024, arXiv e-prints, arXiv:2405.01823, doi: [10.48550/arXiv.2405.01823](https://doi.org/10.48550/arXiv.2405.01823)
- Yang, H., Malhotra, S., Rhoads, J. E., & Wang, J. 2017, *ApJ*, 847, 38, doi: [10.3847/1538-4357/aa8809](https://doi.org/10.3847/1538-4357/aa8809)
- Zou, S., Cai, Z., Wang, F., et al. 2024, arXiv e-prints, arXiv:2402.00113, doi: [10.48550/arXiv.2402.00113](https://doi.org/10.48550/arXiv.2402.00113)